Geoscience Frontiers 10 (2019) 65–76

HOSTED BY

Contents lists available at ScienceDirect

China University of Geosciences (Beijing)

Geoscience Frontiers

journal homepage: www.elsevier.com/locate/gsf

Research Paper

# Nanoscale resetting of the Th/Pb system in an isotopically-closed monazite grain: A combined atom probe and transmission electron microscopy study

A.-M. Seydoux-Guillaume [a,b,*], D. Fougerouse [c,d], A.T. Laurent [a], E. Gardés [e], S.M. Reddy [c,d], D.W. Saxey [c,f]

[a] Univ Lyon, UJM-Saint-Etienne, CNRS, IRD, LMV UMR 6524, F-42023, Saint-Etienne, France
[b] CNRS, Université Clermont Auvergne, IRD, Laboratoire Magmas et Volcans, F-63000, Clermont-Ferrand, France
[c] School of Earth and Planetary Sciences, Curtin University, GPO Box U1987, Perth, WA, 6845, Australia
[d] Geoscience Atom Probe, Advanced Resource Characterisation Facility, John de Laeter Centre, Curtin University, GPO Box U1987, Perth, WA, 6845, Australia
[e] Centre de recherche sur les Ions, les Matériaux et la Photonique (CIMAP), CEA-CNRS-ENSICAEN-UNICAEN, 14070, Caen Cedex 5 France
[f] Department of Physics and Astronomy, Curtin University, GPO Box U1987, Perth, WA, 6845, Australia

ARTICLE INFO

*Article history:*
Received 9 March 2018
Received in revised form
2 July 2018
Accepted 7 September 2018
Available online 9 October 2018

*Keywords:*
Monazite
Nanoscale resetting
Nano-clusters
APM
TEM
UHT metamorphism

ABSTRACT

Understanding the mechanisms of parent-daughter isotopic mobility at the nanoscale is key to rigorous interpretation of U–Th–Pb data and associated dating. Until now, all nanoscale geochronological studies on geological samples have relied on either Transmission Electron Microscope (TEM) or Atom Probe Microscopy (APM) characterizations alone, thus suffering from the respective weaknesses of each technique. Here we focus on monazite crystals from a ~1 Ga, ultrahigh temperature granulite from Rogaland (Norway). This sample has recorded concordant U–Pb dates (measured by LA-ICP-MS) that range over 100 My, with the three domains yielding distinct isotopic U–Pb ages of 1034 ± 6 Ma (D1; S-rich core), 1005 ± 7 Ma (D2), and 935 ± 7 Ma (D3), respectively. Combined APM and TEM characterization of these monazite crystals reveal phase separation that led to the isolation of two different radiogenic Pb (Pb*) reservoirs at the nanoscale. The S-rich core of these monazite crystals contains Ca–S-rich clusters, 5–10 nm in size, homogenously distributed within the monazite matrix with a mean inter-particle distance of 40–60 nm. The clusters acted as a sink for radiogenic Pb (Pb*) produced in the monazite matrix, which was reset at the nanoscale via Pb diffusion while the grain remained closed at the micro-scale. Compared to the concordant ages given by conventional micro-scale dating of the grain, the apparent nano-scale age of the monazite matrix in between clusters is about 100 Myr younger, which compares remarkably well to the duration of the metamorphic event. This study highlights the capabilities of combined APM-TEM nano-structural and nano-isotopic characterizations in dating and timing of geological events, allowing the detection of processes untraceable with conventional dating methods.



## 1. Introduction

The timing of geological processes is fundamental to our understanding of planetary evolution and the events that have shaped the Earth. The most widely used dating technique is based on the radioactive decay of parent U and Th isotopes to their daughter Pb isotopes in accessory minerals such as zircon and monazite. This approach is underpinned by the assumption that both parent and daughter radionuclides are immobile, at the scale of measurement, within the host-mineral lattice. This assumption is commonly violated and disturbance of the isotopic systems has been known for some time (e.g. Wetherill, 1956; Black et al., 1984; Geisler et al., 2003). For example, in the U–Pb system, isotopic disturbance is recognized by a discordance between $^{238}U/^{206}Pb$ and $^{235}U/^{207}Pb$ dates. A small amount of discordance, result in apparently concordant dates, spreading along the concordia curve. Such

* Corresponding author. Univ Lyon, UJM-Saint-Etienne, CNRS, IRD, LMV UMR 6524, F-42023, Saint-Etienne, France.
*E-mail address:* anne.magali.seydoux@univ-st-etienne.fr (A.-M. Seydoux-Guillaume).
Peer-review under responsibility of China University of Geosciences (Beijing).

https://doi.org/10.1016/j.gsf.2018.09.004

distributions are very difficult to interpret because they may represent protracted growth, episodic short-duration growth, or U–Pb disturbance of the geochronometers (e.g. Hawkins and Bowring, 1997; Ashwal et al., 1999; Seydoux-Guillaume et al., 2012; Kirkland et al., 2016; Laurent et al., 2016).

The dating of minerals from rocks that have undergone multiple geological events (polymetamorphism, deformation, alteration, impacts) is often challenging (Corfu, 2013). However, disturbance of the chronometers can be advantageous for investigating complex geological histories. For instance, thermochronology uses the temperature-activated diffusive loss of daughter isotopes from chronometers for constraining the thermal evolution of rocks. The thermochronological approach is however mostly restricted to low-temperature (<300 °C; Reiner and Ehlers, 2005) up to mid-temperature (<650 °C; Smye and Stockli, 2014) environment, precluding the examination of temperature fluctuation in the deep crust ($T$ > 700 °C). Indeed, resetting and closure temperatures of U–Th–Pb in zircon and monazite of typical 100 μm grain diameters are about 1000 °C (Gardés and Montel, 2009), i.e. well above most crustal metamorphic temperatures. The diffusivity of Pb may be dramatically enhanced by defects in the mineral lattice such as radiation damage due to the decay of U and Th (e.g. in zircon, Cherniak and Watson, 2003). However, in contrast to zircon, monazite is not affected by amorphization over time, in spite of alpha decay doses in the range of $10^{19}$–$10^{20}$ α/g, generated by extremely high concentrations of Th (up to 25 wt.% $ThO_2$) and to a lower extent of U (up to 1 wt.% $UO_2$). In monazite crystals, evidence of radiation damage is limited to isolated nm-sized domains within the monazite crystal (Black et al., 1984; Seydoux-Guillaume et al., 2002, 2004), due to alpha-self-healing of radiation damage (Deschanels et al., 2014; Seydoux-Guillaume et al., 2018b). It is therefore generally accepted that radiation damage in monazite is negligible and Pb disturbance at the grain scale (i.e. μscale) is insignificant until high temperature conditions (>1000 °C) are reached.

To date, conventional *in situ* geochemical techniques (EPMA, SIMS, and LA-ICP-MS) have insufficient spatial resolutions (> ~10 $\mu m^3$) for investigating U–Th–Pb disturbances, and more specifically the nanoscale mechanisms. Understanding the mechanisms of parent-daughter isotopic mobility at the nanoscale is however key to rigorous interpretation of U–Th–Pb data and associated dating (Bellucci et al., 2018). Some recent studies have demonstrated that nanoscale characterization is needed to uniquely constrain the mechanisms leading to disturbance of the U–Th–Pb systems. For instance, in ultra-high temperature (UHT) metamorphosed zircon in Archean (Kusiak et al., 2013, 2015) and Proterozoic (Whitehouse et al., 2014, 2017) samples, high spatial resolution (ca. 2 μm) scanning ion imaging has revealed geologically meaningless age variations that are artifacts of the redistributions of radiogenic Pb. Transmission Electron Microscope (TEM) documented that Pb is segregated into Pb-nanospheres, which adversely affected geochronological interpretations due to decoupling of Pb from U (Kusiak et al., 2015, 2018). In addition to TEM, Atom Probe Microscopy (APM) has been shown to be a powerful tool for nanoscale investigations related to trace element, including Pb mobility. Such studies documented evidence of nanoscale Pb mobility in Hadean zircon (Valley et al., 2014), the entrapment of radiogenic Pb in dislocation loops of zircons during high temperature metamorphism (Peterman et al., 2016), Pb and trace element mobility during crystal-plastic deformation of zircon (Piazolo et al., 2016; Reddy et al., 2016) and formation of Ca–Si–Pb-rich phase in monazite during metamorphism (Fougerouse et al., 2018). White et al. (2017) were also able to give accurate U–Pb isotopic analysis of nanoscale domains of baddeleyite by APM. These promising results highlight the potential of TEM and APM studies to characterize nanoscale U–Th–Pb systematics in other minerals; for example, both experimental and natural studies show that the improved geochronological interpretation of monazite necessitates nanoscale observations (e.g. Seydoux-Guillaume et al., 2003, 2018a; Grand'homme et al., 2016, 2018).

To date, all nanoscale geochronological studies on geological samples have relied on either TEM characterization (e.g. Seydoux-Guillaume et al., 2003; Kusiak et al., 2015; Seydoux-Guillaume et al., 2015; Whitehouse et al., 2017) or APM characterizations alone (e.g. Valley et al., 2014, 2015; Peterman et al., 2016; White et al., 2017; Fougerouse et al., 2018). They thus suffer from the respective weaknesses of each technique. APM is a unique technique that combines 3D information, near atomic resolution (0.1 nm in depth) with a chemical sensitivity down to few ppm, and the possibility to obtain isotopic information down to nanometer-scale with typical analyzed volumes of 50 nm × 50 nm × 200 nm (Lefebvre-Ulrickson, 2016). However, it does not provide nanostructural information (e.g. crystallinity, defect, porosity). In contrast, state-of-the-art TEM, enhanced by the recent development of image and probe correctors, HAADF, EDS, monochronomator, and EELS detectors can provide structural and chemical information (e.g. elemental quantification, valence state, local chemical environment …) at the sub-angstrom scale (e.g. Ramasse, 2017). However, TEM does not allow isotope (mass) discrimination, and cannot quantify minor and trace elements at less than wt.% concentrations.

The combination of APM and TEM, either on exactly the same sample (i.e. correlative microscopy) or not, was only recently achieved in both material sciences (e.g. Grenier et al., 2014, 2015; Bonef et al., 2015; Lefebvre-Ulrickson, 2016) and geosciences (e.g. Weber et al., 2016; Rout et al., 2017); however, to our knowledge, it is the first time that it is applied for geochronology. Here we combine APM and TEM to demonstrate that disturbance and even resetting of Th–Pb system in UHT metamorphic monazites from Rogaland (Norway) can occur by diffusion at nanoscale even though apparently undisturbed at grain-scale. We show that dating and timing of a metamorphic event is possible by combined TEM-APM investigations of sub-micrometric domains of chronometers, opening the way for nano-geochronology and nano-thermochronology.

## 2. Geological and sample context

Rogaland (S-Norway) underwent a protracted metamorphic and magmatic evolution in the course of Sveconorwegian orogeny (1140–900 Ma; Bingen et al., 2008; Slagstad et al., 2013). Two distinct metamorphic phases peaking at UHT are recognized, at ca. 1030–1005 Ma and ca. 930 Ma (Möller et al., 2002; Drüppel et al., 2013; Laurent et al., 2018a). The first metamorphic phase (M1) followed a clockwise $P$–$T$ path reaching UHT condition of 900–950 °C and 0.5–0.6 GPa, while the second phase of metamorphism (M2) occurred at slightly lower $P$ of ca. 0.4 GPa and similar temperatures of 900 °C (Blereau et al., 2017; Laurent et al., 2018a). These two phases are spatially superimposed in the so-called UHT zone, resulting in protracted melting and temperatures above 800 °C over more than 100 My (1040–930 Ma) as recorded by zircon U–Pb geochronology coupled to Ti-in-zircon thermometry (Laurent et al., 2018b). Finally, M2 retrograde isobaric cooling is documented by an average titanite U–Pb age of 918 ± 2 Ma (Bingen and Van Breemen, 1998) and an average amphibole $^{40}Ar$–$^{39}Ar$ age of 916 ± 14 Ma (Bingen et al., 1998).

In this study, we reinvestigate monazite crystals from an osumilite gneiss, sampled within the UHT zone (*ALR 13-58*; UTM coordinates *x:* 332482, *y:* 6503981), which have been previously characterized in Laurent et al. (2016) and Seydoux-Guillaume et al. (2018a). Three main textural domains have been identified in the monazite crystals, based on their microchemistry and presence of solid and fluid

inclusions: (1) a S-rich core D1 (0.4 at.% S) (2) secondary S-bearing domains D2 (S > 0.05 at.%, partly clouded with solid inclusions), and (3) late S-free, Th-rich domains (1.1–1.5 at.% Th). Sulphur has been shown to be primarily incorporated in monazite lattice as an anhydrite component ($Ca^{2+} + S^{6+} = REE^{3+} + P^{5+}$ substitution). TEM imaging revealed that domain D1 contains nanoclusters (5–10 nm) enriched in Ca and S that were interpreted as the result of homogenous exsolution of the anhydrite component in the host monazite. This sample records apparently concordant U–Pb dates (measured by LA-ICP-MS) that range over 100 My, with the three domains yielding distinct isotopic U–Pb ages of 1034 ± 6 Ma (D1), 1005 ± 7 Ma (D2), and 935 ± 7 Ma (D3), respectively (Laurent et al., 2016, Table 1). From the petrological context, it has been proposed that S-rich monazite cores (D1) crystallized at 1034 ± 6 Ma during M1 fluid-absent partial melting. The occurrence of secondary S-bearing domains (D2), clouded with solid inclusions, is interpreted to results from a dissolution–precipitation event dated at 1005 ± 7 Ma, which marks the end of M1 UHT phase. The transition from oxidized to reduced metamorphic conditions between M1 and M2 is also recorded by the crystallization of molybdenite ($MoS_2$) at 973 ± 4 Ma (Bingen and Stein, 2003). Finally, the S-free D3 monazite domains crystalized at 935 ± 6 Ma, corresponding to M2 UHT phase (more details are given in Laurent et al., 2016).

## 3. Methods

### 3.1. Electron probe micro analysis (EPMA)

In situ micro-chemical analysis and dating (Fig. 1) were acquired using a Cameca SX-FIVE electron probe microanalyser (EPMA) hosted at the Raimond Castaing micro-characterization centre (Toulouse, France). The EPMA was operated with a focused beam at standard operating conditions of 15 kV and 20 nA for point analyses and 200 nA for dating. Analytical details, including reproducibility, are given in Laurent et al. (2016). The age and associated confidence interval were calculated following Montel et al. (1996) with the R-package NileDam (Seydoux-Guillaume et al., 2012; Villa-Vialaneix et al., 2013).

### 3.2. Focused ion beam (FIB)

Three focused ion beam (FIB) foils were prepared for TEM analyses by the *in-situ* lift-out technique, on a FEI dual-beam microscope (Hélios600i) at the LAAS laboratory in Toulouse (Laurent et al., 2016). Seven atom probe specimens were prepared from the three specific domains of the monazite grain. The APM sample preparation was performed using the Tescan Lyra3 dual Focused Ion Beam Scanning Electron Microscope (FIB-SEM) at Curtin University using the lift-out method described in detail elsewhere (Fougerouse et al., 2016; Peterman et al., 2016). The ion beam was operated at 30 kV during the procedure with a final low voltage (2 kV) stage being used to remove the effects of Ga implantation created by the high-energy Ga beam.

### 3.3. Transmission electron microscopy (TEM)

Focused ion beam (FIB) foil, prepared by the in-situ lift-out technique (details in Laurent et al., 2016), were examined with a JEOL cold FEG ARM200F TEM operated at 200 kV, equipped with a Cs corrector, EDS, STEM HAADF detector, and a GIF QUANTUM (more details in Laurent et al., 2016). Chemical mapping (Ca, S, P and Ce) were also performed in STEM mode with a Titan Themis 300 equipped with a Cs corrector and the SuperX EDS system at 60 kV, 100 pA and during 8 min (Fig. 2).

### 3.4. Atom probe microscopy (APM)

APM allows quantification in 3D of trace element and isotopic abundances with sub-nanometre resolution (Thompson et al., 2007; Gault et al., 2012; Kelly and Larson, 2012; Gault et al., 2016). All species are identified by time-of-flight spectrometry, and are ranged based on mass, charge state (1+ to 3+), and relative isotopic abundances (Fig. 3). Spatial information is reconstructed using the *x-y* impact location of the ionic species on the position sensitive detector and the order of impact succession (Gault et al., 2012; Kelly and Larson, 2012).

Atom probe Microscopy analyses were undertaken on the Advanced Resource Characterisation Facility's Geoscience Atom Probe (Cameca LEAP4000X HR) housed in the John de Laeter Centre, Curtin University, Perth, Australia. The instrument was operated in laser mode with a UV laser ($\lambda = 355$ nm), pulse energy of 100 pJ, base specimen temperature of 50 K and evaporation rate of 0.01 atom/pulse. The instrument variables and reconstruction parameters are given in Supplement Table S1 following recommendations of Blum et al. (2018). IVAS v3.6.14 processing software was used to analyse and display the data. In order to minimise the mixing of the chemistry of different domains, a 2.5 at.% Ca isoconcentration surface (Hellman et al., 2000) was used to calculate the composition of the matrix, with a 5 at.% Ca isoconcentration surface used to extract the composition of the clusters. Proximity histograms representing the composition of the monazite from the centre of the cluster to a maximum radius of 10 nm with a fixed binning of 0.1 nm were used to investigate the composition transition between the cluster and the host (Hellman et al., 2000).

The total major and trace elements composition of the monazite was calculated using the full width of the peaks, whereas the isotopic quantification of Pb and Th was measured using a narrow range of fixed width (0.1 Da) to eliminate peak interferences on the thermal tail of the $ThO^{++}$ peak as recommended previously (Fougerouse et al., 2018). $^{206}Pb^{++}$ and $^{208}Pb^{++}$ were identified at 103 Da and 104 Da respectively (Fig. 3). Th is present, primarily as $ThO^{++}$ (~120 Da), but also as $ThPO_3^{+++}$ (~103.7 Da), $ThPO_4^{++}$ (~163.5 Da) and as $ThP_2O_6^{+++}$ (~234 Da). A 0.1 Da fixed width was used for ranging each isotopic species and background counts were subtracted from each peak. Background counts were estimated for each analysis by measuring the noise level in proximity of each quantified species. Uncertainties

**Table 1**
Representative composition and age of the investigated monazite domains measured by EPMA and LA-ICP-MS from Laurent et al. (2016) and this study.

| Domain | Concentration (at.%) from EPMA (this study) | | | | | Isotopic ratios | (LA-ICP-MS)[a] | LA-ICP-MS U-Pb age[a] (±2σ) | EPMA U-Th-Pb date[a] (±2σ) | U-Th-Pb date (this study) |
|---|---|---|---|---|---|---|---|---|---|---|
| | Ca | S | Th | U | Pb | $^{208}Pb/^{206}Pb$ | ±1σ | | | |
| D1 (M15-16) | 1.043 | 0.439 | 0.707 | 0.022 | 0.041 | 10.23 | 0.2 | 1034 ± 6 | 1028 ± 8 | 1037 ± 19 |
| D2 (M18-19) | 0.793 | 0.097 | 1.200 | 0.017 | 0.063 | 26.67 | 0.4 | 1005 ± 7 | 998 ± 6 | 995 ± 14 |
| D3 (M22) | 0.259 | <0.03 | 1.489 | 0.013 | 0.073 | 26.35 | 0.3 | 935 ± 7 | 952 ± 6 | 941 ± 11 |

Rq: Isotopic ratios are derived from single LA-ICP-MS analysis located the closest to the FIB foils used in this study whereas quoted LA-ICP-MS and EPMA ages are pooled ages reported in Laurent et al. (2016).
[a] data from Laurent et al. (2016).

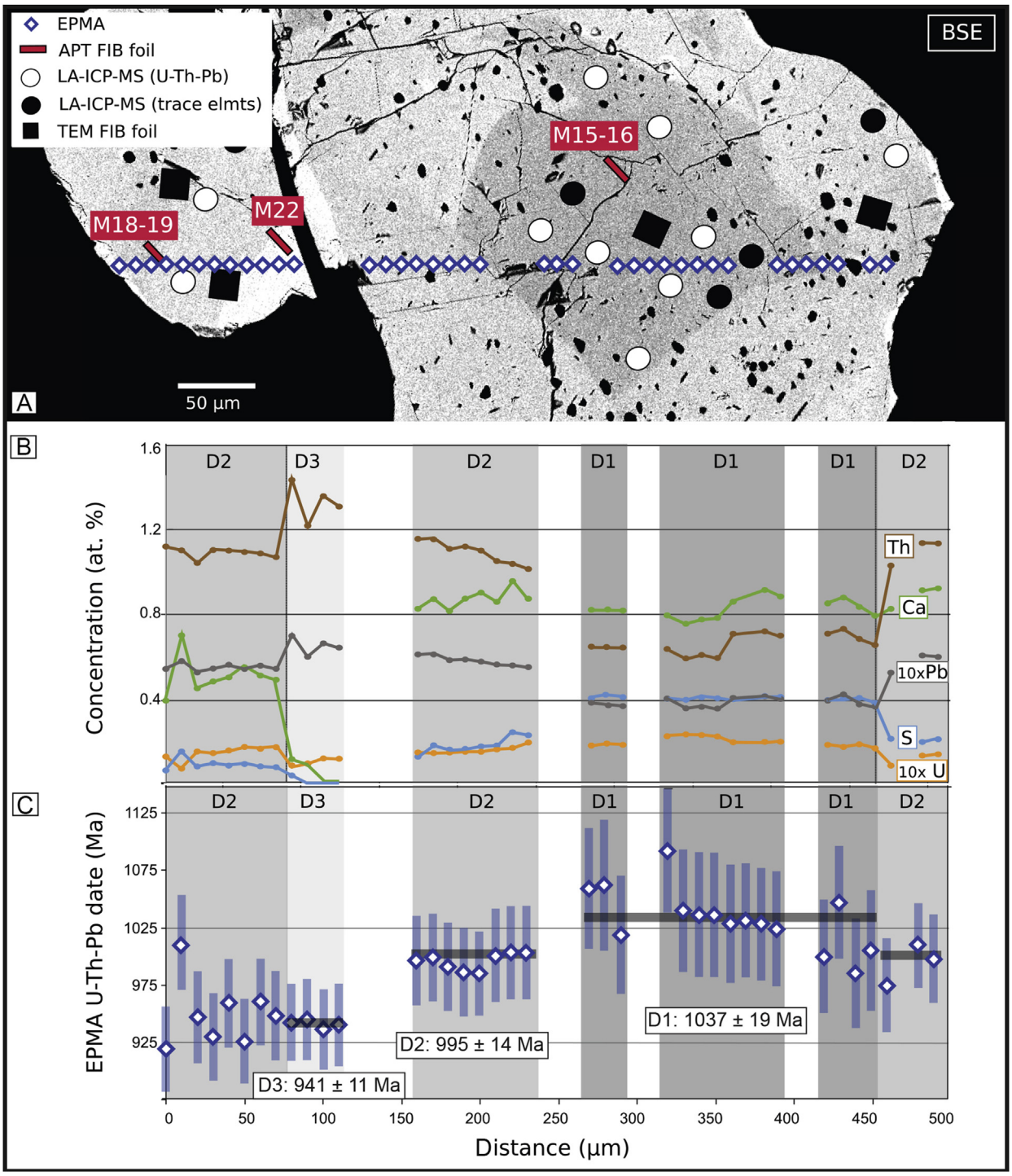


**Figure 1.** Microscale characterization of the studied monazite crystal, including (A) BSE imaging, (B) EPMA micro-chemistry and (C) EPMA total-Pb dating. (A) High-contrast BSE image of the studied monazite crystal with the location of LA-ICP-MS analyses reported in Table 1 and location of TEM and APM FIB foils. The dark inclusions in monazite are solid and fluid inclusions; Compositional traverse across the grain for selected elements in at.% (B) and EPMA total-Pb ages in Ma (C). The vertical errors bars on (C) are drawn at 95% confidence level.

for each background-corrected species were calculated by adding the counting statistics uncertainty for each isotope peak and the counting statistics uncertainty for its correction in quadrature. The uncertainties in isotopic ratios were subsequently propagated from the uncertainty of each species and reported at 1$\sigma$ (Table 2).

In order to increase the precision of the quantification and the number of atoms for each domain, all the clusters within each specimen were combined. Despite this approach, the count of certain atomic species, in particular $^{206}Pb^{++}$ remains very low (11–14 atoms/specimen).

## 4. Results

### 4.1. Micro-chemical characterization with EPMA

Micro-characterization by EPMA of one selected monazite crystal (Fig. 1A and B, Supplement Table S2) confirms that three chemical domains may be distinguished as (1) a S-rich core D1 (0.4 at.% S), (2) secondary S-bearing domains D2 (S > 0.05 at.%, partly clouded with solid inclusions), and (3) late S-free, Th-rich domains (1.1–1.5 at.% Th). In order to benefit from a smaller sampling volume (ca. 3 $\mu m^3$) and accurate Th, U and Pb concentrations, EPMA total-Pb dating (essentially Th–Pb) was performed along a traverse in the grain with a 10 μm step (Fig. 1C). Overall, EPMA total-Pb dates of 1037 ± 19 Ma for D1, 995 ± 14 Ma for D2 and 941 ± 11 Ma for D3 are in perfect agreement with published U–Pb isotopic and total-Pb ages from Laurent et al. (2016) (Table 1).

### 4.2. Nano-structural and chemical characterization with TEM

Nano-structural and chemical characterization with TEM in the S-rich core (D1 domain; Fig. 1), confirm the presence of Ca–S-rich nanoclusters. Such clusters are absent from the other domains (D2 and D3) of the monazite crystal. They are easily detected with STEM-HAADF detector (Fig. 2A and B). They form 5–10 nm sized black dots, representing a negative density contrast, and are homogenously distributed all over the foil, with a mean interparticle distance of 40–60 nm. High magnification images, with a [101] zone axis orientation, record a number of features that aid interpretation of cluster formation. High resolution dark field (DF) imaging (Fig. 2C) reveals the arrangement of atomic columns composed of heavy elements, mostly light rare earth element (LREE) chains (Ni et al., 1995), in the sample volume. High resolution bright field (BF) imaging (Fig. 2D) shows the atomic arrangement of lighter elements (e.g. P and O atoms), with little lattice misorientation associated with the presence of the Ca–S-rich nanocluster. Energy-dispersive spectroscopy (EDS) mapping acquired across some nanoclusters (two are distinctly identified) reveal that they are enriched in Ca and S and depleted in Ce and P (Fig. 2E) compared with the host monazite. However, such mapping or TEM-EDS analyses cannot detect chemical elements in concentrations lower than ~1 wt.%, including U or Pb, and do not allow the analysis of such small domains without analysing the matrix of the TEM-foil.

### 4.3. Nano-chemical and isotopic characterization with APM

Atom probe results are summarized in Table 2 and reported in detail in Supplement Tables S2 and S3 and Fig. S1. Five atom probe needles were analysed from three different domains (D1–D3) of the monazite crystal (Fig. 1); each tip yielded 16–34 million atoms (Table 2). The mass spectrum for monazite is very complex due to the presence of single ion species and complex molecular species of LREE and P with different charge states (Fig. 3). The quantification of monazite composition by APM is thus not straightforward, in line with the first APM results on monazite published by Fougerouse et al. (2018). The composition of monazite derived by APM data (at.% in Table 2 and Supplement Table S2) show depletion in O (~8%) and P (16%) and excess in LREE (e.g. up to 60% for Ce but less than 6% for Nd) compared to expected stoichiometry and analyses obtained at the micron-scale using EPMA (Table 1 and Supplement Table S2).

The $Pb_{total}$ and Th concentration measured by APM, using the full width of the peaks, and EPMA are in good agreement (Tables 1 and 2). As an example, the domain D3 (cluster free) yielded concentrations of 1.489 at.% Th and 0.073 at.% Pb with EPMA (Table 1) and 1.439 at.% Th and 0.085 at.% Pb with APM (Table 2), which correspond to differences of 3.4% and 17% respectively (Supplement Table S2). $^{208}Pb/^{232}Th$ isotopic ratios measured by APM are systematically higher (~30%) than measured with LA-ICP-MS (but

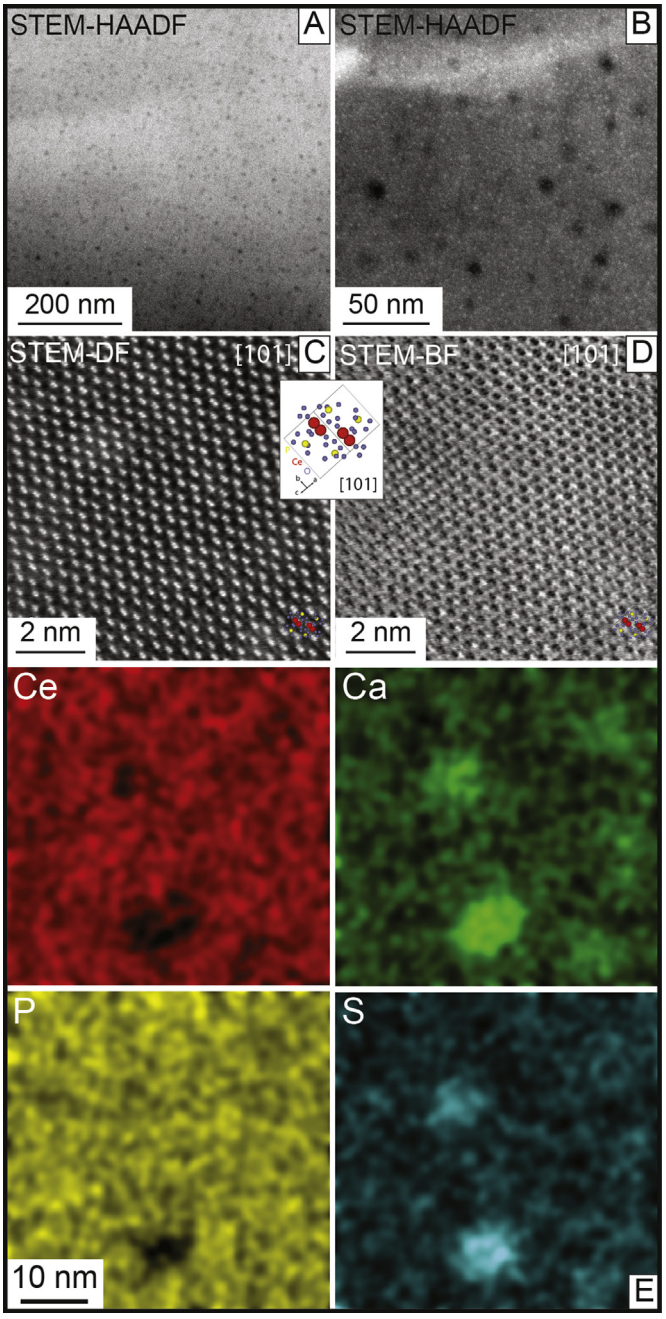


**Figure 2.** Scanning Transmission Electron Microscope (STEM) images in Dark Field (A–C) or Bright Field mode (D) and EDS-chemical maps (E). (A, B) STEM-DF images (with High Angle Annular Dark Field detector-HAADF) at low magnification. The *black dots* homogeneously distributed in the volume and corresponding to negative density contrasts, are Ca–S-clusters. (C, D) Zoom in one cluster within monazite matrix in [101] zone axis. In DF mode (C) only atomic columns with heavy elements (e.g. Ce chains) are visible and appears bright (C); in BF mode only light elements (e.g. P, O) appears bright (D). A simplified representation of $CePO_4$ monazite structure is shown in inset (Red balls: Ce, Yellow: P and purple: O). (E) Ce, Ca, S, P-EDS maps across few Ca–S-rich nanoclusters (the biggest one in the figure is ~10 nm in size) showing depletion in Ce and P and enrichment in Ca and S. Bright spots in (A) and (B) correspond to Ga implantation during sample preparation. Note that these 10 nm-clusters are distributed in a ~100 nm thick sample, i.e. there is always a contribution of the matrix during TEM analyses (image or mapping).

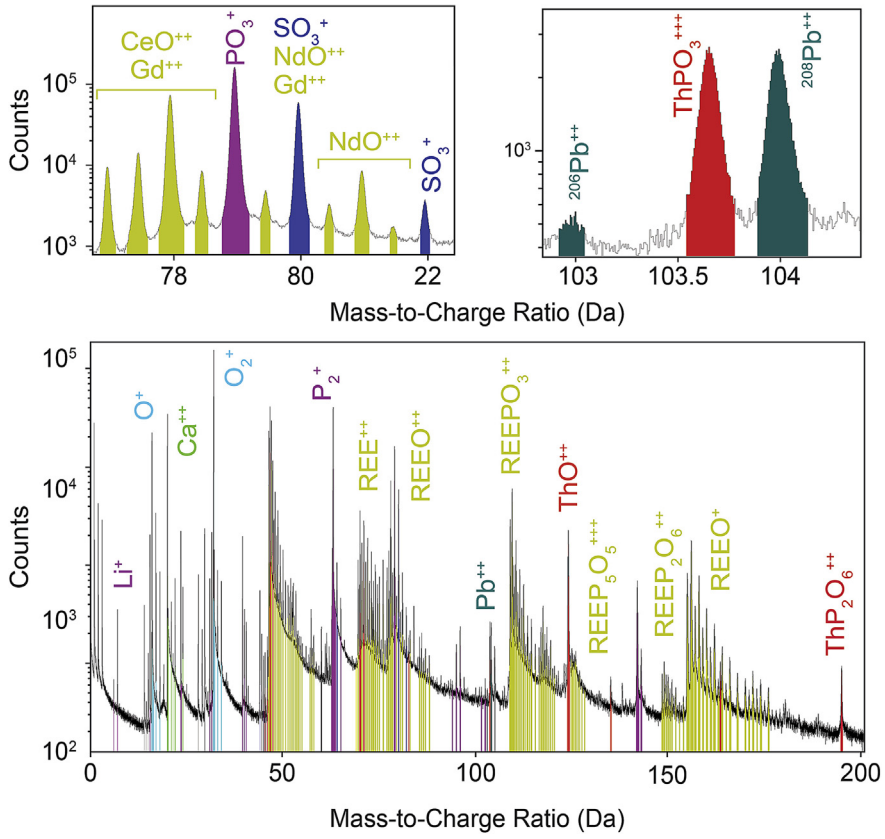


**Figure 3.** Atom probe mass spectrum. Peaks are color-coded by atomic or molecular species. Details of the mass spectrum showing the position of the $SO_3^+$, $CeO^{++}$, $Gd^{++}$, $NdO^{++}$, $^{206}Pb^{++}$, $^{208}Pb^{++}$ and $ThPO_3^{+++}$ peaks.

also when compared to Pb/Th ratios measured by EPMA). As a consequence, raw APM $^{208}Pb/^{232}Th$ ratios yield systematically and significantly overestimated ages of 1373 ± 14 Ma, 1347 ± 10 Ma, and 1332 ± 14 Ma for D1, D2 and D3 respectively (Tables 1 and 2).

Spatially reconstructed atom probe data from two tips (~20 million atoms), representative of all analysed tips, are presented in Fig. 4: one from domain D1 (tip M15; Fig. 4A and Supplement Fig. S1) and one from domain D3 (tip M22; Fig. 4B and Supplement Fig. S1). All specimens from domains D2 and D3 show homogeneous distributions of all elements, especially Ca, S and Pb (Fig. 4B and Supplement Fig. S1). In contrast, APM data from S-rich domains D1 i.e. tips M15 and M16 (Table 2), confirm the presence of nanoclusters (5–10 nm) enriched in Ca, S, U and Pb and depleted in P, Ce and Th compared to the monazite matrix (Figs. 4 and 5, Table 2), in agreement with TEM results. The Ca, S, Pb and U concentration increase from ~1.4, ~0.8, ~0.05 and 0.017 at.% in the matrix to 9.2, 5.7, 0.11 and 0.022 at.% inside the clusters, respectively (Table 2); in contrast Th, P, REE (i.e. Ce) decreases from ~0.7, 13.6, and 9.8 at.% within the matrix to ~0.5, 9.3, and 6.3 at.% respectively (Supplement Table S2).

The measured $^{208}Pb/^{232}Th$ ratios are much higher in the clusters compared to the matrix (~0.23 vs. ~0.07; Fig. 6A, Table 2) leading to unrealistic $^{208}Pb/^{232}Th$ dates (~4 Ga vs. ~1.3 Ga).

## 5. Discussion

### 5.1. Dating monazite with atom probe

It is obvious that the ~1.3 Ga ages calculated from $^{208}Pb/^{232}Th$ ratios measured by APM are overestimated when compared to ages obtained by LA-ICP-MS and EPMA (see Tables 1 and 2). A similar relationship was previously observed in the first APM investigations on monazite (Fougerouse et al., 2018). The high $^{208}Pb/^{232}Th$ ages can be the result of an overestimation of the $^{208}Pb$ content or an underestimation of the Th composition. On the mass spectrum (Fig. 3), a $ThPO_3^{+++}$ peak at 103.66 Da is clearly distinguishable from the $^{208}Pb^{++}$ peak (103.99 Da) and therefore cannot account for an increased $^{208}Pb$ quantification. In zircon, a $Si_2O_3^+$ peak at 103.939 Da directly overlaps with $^{208}Pb^{++}$ independently of running conditions (Saxey et al., 2018). However, the low Si content in the studied monazite (0.3–1.2 at.%; Supplement Table S1) indicates that this overlap should be negligible compared to zircon. Th is in majority present as $ThO^{++}$ in the mass spectrum (Fig. 3), but also as $ThPO_3^{+++}$, $ThPO_4^{++}$ and as $ThP_2O_6^{+++}$. To overcome the overlap between the thermal tail of $ThO^{++}$ and $P_5O_5REE^{+++}$ molecules, Fougerouse et al. (2018) suggested to use a fixed, narrow (0.1 Da) range width in order to compare the peak height of the species used for the calculation of the $^{232}Th$ and $^{208}Pb$ composition. However, this approach is valid only if the shape of each peak used for the isotopic composition is comparable and more work is necessary to define whether this assumption can be validated. Finally, A Th-bearing molecule may have been misidentified in the mass spectrum resulting in missed counts. Reliable compositions and $^{208}Pb/^{232}Th$ age calculations by atom probe require then a complete elemental calibration, which will be the objective of a future study. We however propose a correction of APM ages by calibrating them with LA-ICP-MS and EPMA ages. We tentatively applied a linear least squares regression of LA-ICP-MS and EPMA ages of D1, D2 and D3 domains as a function of corresponding bulk APT ages (Supplement Table S4). The calibration provides corrected ages deviating from LA-ICP-MS and EPMA ages by 14 Ma on average

**Table 2**
Chemical and isotopic analysis from APT tips prepared from three different domains (D1, D2 and D3) in S-rich monazite crystal described in Fig. 1. Corrected APT dates are calculated by calibrating raw APT dates with LA-ICP-MS and EPMA dates, and errors include both date measurements and calibration fit errors (see Text and Supplemental Table S3).

| | APT-Tip | Atom nb | Domain | Concentrations (at.%) | | | | | | | | | $^{208}Pb/^{206}Pb$ ratios | | $^{208}Pb/^{232}Th$ ratios | | $^{208}Pb/^{232}Th$ dates | | $^{208}Pb/^{232}Th$ corrected dates | |
|---|---|---|---|---|---|---|---|---|---|---|---|---|---|---|---|---|---|---|---|---|
| | | | | Th | ±1σ | U | ±1σ | Pb | ±1σ | Ca | ±1σ | S | ±1σ | | ±1σ | | ±1σ | | ±1σ | | ±1σ |
| D1 | M15 | 20M | Bulk | 0.678 | 0.002 | 0.017 | 0.0003 | 0.051 | 0.0004 | 1.511 | 0.002 | 0.791 | 0.002 | 10.2 | 1.2 | 0.0703 | 0.0011 | 1374 | 22 | 1038 | 21 |
| | | | Matrix 2.5 | 0.683 | 0.002 | 0.017 | 0.0003 | 0.049 | 0.0004 | 1.386 | 0.002 | 0.714 | 0.002 | 10.3 | 1.2 | 0.0680 | 0.0011 | 1330 | 22 | 955 | 21 |
| | | | Clusters 5 | 0.485 | 0.017 | 0.022 | 0.0040 | 0.096 | 0.0070 | 9.145 | 0.076 | 5.583 | 0.058 | 10.3 | 6.6 | 0.2427 | 0.0291 | 4391 | 479 | | |
| | M16 | 27M | Bulk | 0.694 | 0.001 | 0.017 | 0.0002 | 0.048 | 0.0004 | 1.443 | 0.002 | 0.905 | 0.002 | 10.3 | 1.0 | 0.0702 | 0.0010 | 1372 | 18 | 1034 | 19 |
| | | | Matrix 2.5 | 0.698 | 0.001 | 0.017 | 0.0002 | 0.047 | 0.0004 | 1.339 | 0.002 | 0.839 | 0.002 | 10.5 | 1.0 | 0.0684 | 0.0010 | 1337 | 18 | 968 | 19 |
| | | | Clusters 5 | 0.471 | 0.017 | 0.022 | 0.0040 | 0.124 | 0.0090 | 9.168 | 0.078 | 5.915 | 0.062 | 7.7 | 3.7 | 0.2307 | 0.0276 | 4197 | 459 | | |
| | *Mean* | | *Bulk* | *0.686* | *0.001* | *0.017* | *0.0002* | *0.050* | *0.0003* | *1.477* | *0.001* | *0.848* | *0.001* | *10.2* | *0.8* | *0.0703* | *0.0007* | *1373* | *14* | *1036* | *14* |
| | | | *Matrix 2.5* | *0.691* | *0.001* | *0.017* | *0.0002* | *0.048* | *0.0003* | *1.363* | *0.001* | *0.777* | *0.001* | *10.4* | *0.8* | *0.0682* | *0.0007* | *1333* | *14* | *962* | *14* |
| | | | *Clusters 5* | *0.478* | *0.012* | *0.022* | *0.0028* | *0.110* | *0.0057* | *9.157* | *0.054* | *5.749* | *0.042* | *9.0* | *3.8* | *0.2367* | *0.0201* | *4294* | *332* | | |
| D2 | M18 | 16M | Bulk | 1.208 | 0.002 | 0.010 | 0.0002 | 0.076 | 0.0006 | 1.111 | 0.002 | 0.635 | 0.002 | 16.7 | 2.3 | 0.0692 | 0.0009 | 1352 | 17 | 997 | 18 |
| | M19 | 34M | Bulk | 1.265 | 0.002 | 0.011 | 0.0002 | 0.079 | 0.0004 | 1.178 | 0.002 | 0.640 | 0.001 | 30.6 | 4.9 | 0.0687 | 0.0006 | 1343 | 12 | 979 | 16 |
| | *Mean* | | *Bulk* | *1.237* | *0.001* | *0.011* | *0.0001* | *0.078* | *0.0004* | *1.145* | *0.001* | *0.638* | *0.001* | *23.7* | *2.7* | *0.0689* | *0.0006* | *1347* | *10* | *988* | *12* |
| D3 | M22 | 20M | Bulk | 1.439 | 0.002 | 0.004 | 0.0001 | 0.085 | 0.0006 | 0.418 | 0.001 | 0.459 | 0.001 | 87.2 | 43.2 | 0.0681 | 0.0007 | 1332 | 14 | 959 | 17 |

(root mean square error), i.e. less than 2% (see Tables 1 and 2). Since our calibration is made on dates spanning over 100 Myr around 1 Ga only, and for a narrow range of Th and Pb concentrations, the extrapolation outside these ranges may not be valid. Corrected ages were not calculated for clusters for that reason. However, this simple linear regression provides calibrated APM Th–Pb ages in monazite in good agreement with LA-ICP-MS and EPMA ages (see Tables 1 and 2). This indicates that APM age (and composition) calibration should be attainable, introducing Th-Pb nano-geochronology with APM as a new dating technique for monazite at the nanoscale.

### 5.2. Cluster formation and role as Pb sink

When compared to the D1 monazite matrix, the clusters have higher Pb concentrations but lower total radioactive isotopes (e.g. Th; Fig. 6B). This indicates that Pb is chemically more favourable in the clusters and there is an excess of Pb that does not originate from the decay of Th and U contained in the clusters (Fig. 6A). Given the Th, U and Pb concentrations of the clusters (Table 2) and the age of D1 monazite (~1.03 Ga), approximately 25% of Pb content in the clusters is radiogenic and ~75% is in excess. If the clusters were primary features related to nucleation (e.g. Helmy et al., 2013), the incorporated Pb would carry an inherited signature (i.e. common Pb) and be incorporated as a cheralite-like (Ca,Pb,Th) $(PO_4)_2$ component (Montel et al., 2002; Clavier et al., 2011). However, a mixture of 25% radiogenic Pb ($^{208}Pb/^{206}Pb = 6.5$ after 1 Ga) with 75% common Pb (terrestrial $^{208}Pb/^{206}Pb = 2.16$ at ~1 Ga; Stacey and Kramers, 1975) yields a $^{208}Pb/^{206}Pb_{calc}$ of 3.3, which is well below the $^{208}Pb/^{206}Pb_{measured}$ value of 9.0 ± 3.8 detected in the clusters by APM. It is therefore unlikely that Pb content in the clusters stems from a primary enrichment in common Pb. This is in line with previous LA-ICP-MS analyses by Laurent et al. (2016) which did not reveal measurable common Pb in D1 monazite. Note that even if the error on $^{208}Pb/^{206}Pb_{measured}$ is rather large, it is unlikely that this measurement is biased since it is the ratio of two isotopes of the same element, contrary to $^{208}Pb/^{232}Th$ ratios. Indeed, the $^{208}Pb/^{206}Pb$ of bulk D1 monazite measured by APM is in remarkable agreement with LA-ICP-MS measurement (10.2 ± 0.8 vs. 10.23 ± 0.20; Tables 1 and 2).

Radiogenic Pb signature in bulk D1 monazite 100 Myr after crystallization is calculated to be such that $^{208}Pb/^{206}Pb_{calc}$ is about 11.5, when considering Th and U concentration measured by APM. Recalling that 25% of Pb content in the clusters is radiogenic Pb produced in clusters and assuming the remaining 75% come from Pb produced in the host monazite (bulk D1), yields a $^{208}Pb/^{206}Pb_{calc}$ value of 10.2 in the clusters, in good agreement with measured values (9.0 ± 3.8). Thus, excess Pb in the clusters is consistent with derivation from the radiogenic Pb produced in the host monazite. Therefore, our preferred model is that an initially Ca–S-rich monazite, containing ~1.04 at.% Ca and ~0.44 at.% S (EPMA composition of monazite D1; Table 1; Laurent et al., 2016; Seydoux-Guillaume et al., 2018a), underwent exsolution to form the Ca–S enriched clusters at given temperature. The absence of experimental data on the miscibility gap between monazite and anhydrite means that the pressure-temperature (P–T) conditions at which the anhydrite component exsolved from the monazite cannot be specified. However, the absence of Ca–S-rich clusters in D2 monazite, which also contains a Ca–S-component (0.097 at.% S; Table 1) but formed at lower temperature than D1, indicate that cluster formation in D1 probably took place during cooling after the first temperature peak. The preservation of the exsolution products, despite heating of the sample during M2 (Laurent et al., 2016), may reflect the temperature remaining below the solvus during M2, modification of the solvus position due to the lower pressure

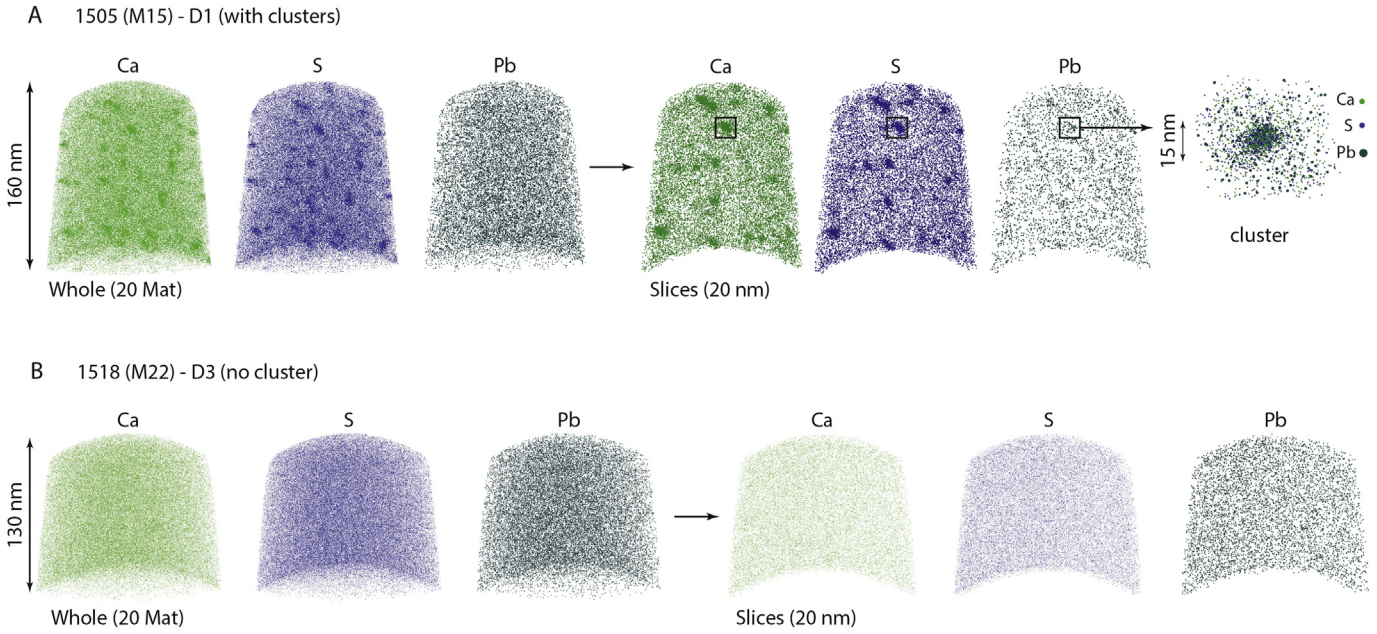


**Figure 4.** Reconstructed three-dimensional atom probe microscopy (APM) images of Ca, S and total Pb distribution in sample M15 (1505) prepared from cluster-rich-D1 domains (A) and sample M22 (1518) from cluser-free-D3 domains (B). Each sphere represents one atom. Slices (20 nm thick) from these 3D-images are also presented and a close up of one cluster in (A).

conditions of M2 (Laurent et al., 2016, 2018b; Blereau et al., 2017), change in the REDOX state (more reduced conditions after M1) or kinetic issues.

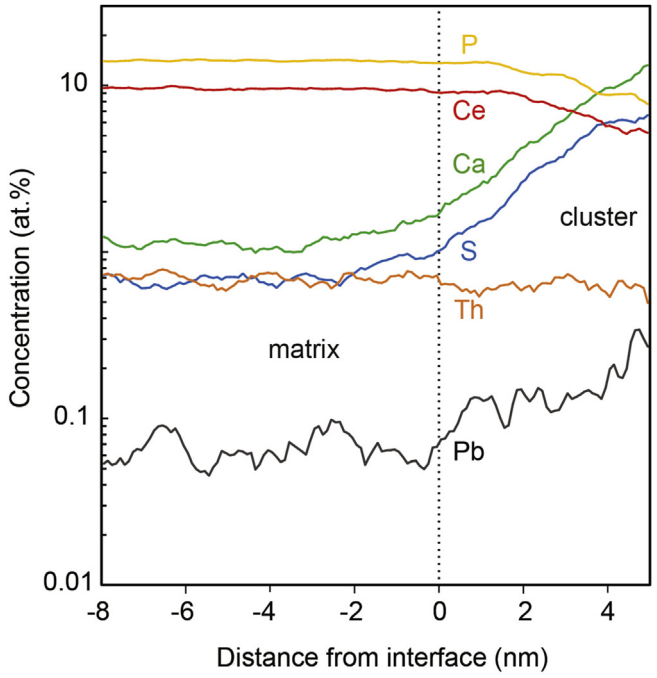


**Figure 5.** Proximity histogram (proxigram for short) concentration profile (smoothing is applied with taking a moving average on 8 distance steps of 0.05 nm) based on a 2.5 at.% Ca isoconcentration surface (distance 0 represents the edge of the isosurface). The histogram shows the increase in Ca, S and Pb and decrease in P, Ce and Th over 5 nm. Positive *x*-axis values represent the distance (in nm) between the 2.5 at.% Ca isoconcentration surface and the centre of the cluster, whereas negative values represent matrix monazite. In APM measurements, this gradual chemical variation typically arises from ion trajectory aberrations (local magnification effect) during analysis of polyphased materials and can also induce modifications in both the chemistry and shape of the inclusion (Vurpillot et al., 2000; Fougerouse et al., 2016).

### 5.3. Nanoscale resetting of Th/Pb system in grain-scale closed system

D1 monazite formed near the first peak of UHT metamorphism (M1) while D3 monazite formed at the second peak (M2) some

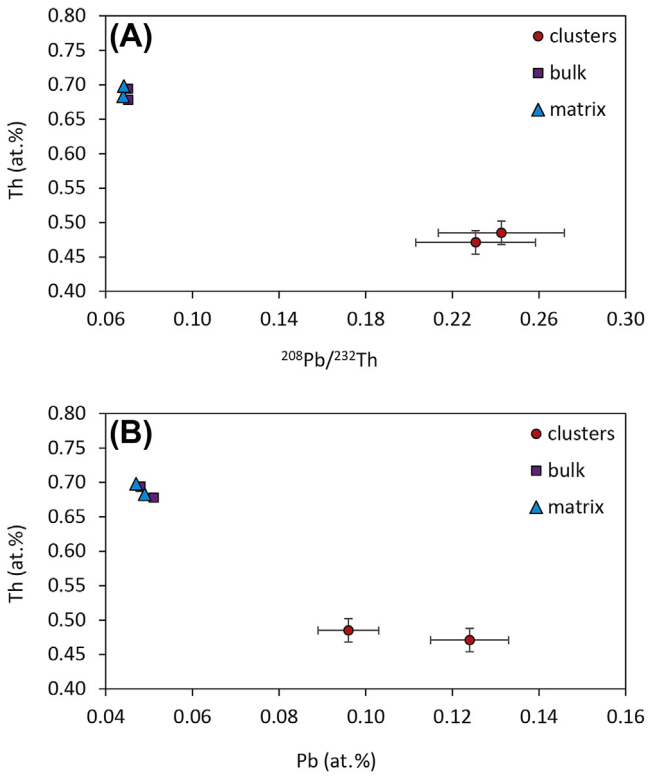


**Figure 6.** APM concentrations of Th (in at.%) plotted versus $^{208}Pb/^{232}Th$ ratios in (A), and versus Pb concentrations (in at.%) in (B) from both APM tips prepared in D1-domain (Table 2). Clusters (in red) are enriched in Pb and depleted in Th compared to the bulk (purple) and the matrix (blue).

~100 Myr later (Table 1) with minimum temperature of ~750–800 °C in-between, indicated by Ti-in-zircon thermometry (Laurent et al., 2018b). Since (1) the clusters act as sinks for Pb, and (2) the age of the matrix of D1 monazite is similar to that of D3 monazite, it appears that the clusters induced the continuous, nano-scale, resetting of the matrix of D1 monazite over the high-T metamorphic evolution (M1–M2), while the bulk grain remained closed. It is important to notice that this is independent from age correction since the raw $^{208}Pb/^{232}Th$ ratio of matrix of D1 is identical to that of D3 (Table 2). Continuous resetting is in good agreement with experimentally derived diffusion coefficient of Pb in monazite (Cherniak et al., 2004; Gardés et al., 2006, 2007). Temperatures of 950–800 °C are (however) insufficient for resetting a monazite grain of several hundreds of μm in size. For instance, the durations required for Pb to diffuse over 100 μm at 900 and 800 °C are ~6 Gyr and ~600 Gyr respectively (Gardés et al., 2006, 2007). On the other hand, Pb diffusion at the cluster scale (~20 nm) is virtually instantaneous at these temperatures. The durations required for Pb to diffuse over 25 nm, i.e. about the mean half distance between the clusters, are ~0.0004 Myr and ~0.04 Myr at 900 and 800 °C, respectively. Thus, the nanoscale matrix system can be continuously reset and the clusters gain unsupported Pb while the microscale bulk grain system remains closed. Nanoscale resetting should have then stopped at about

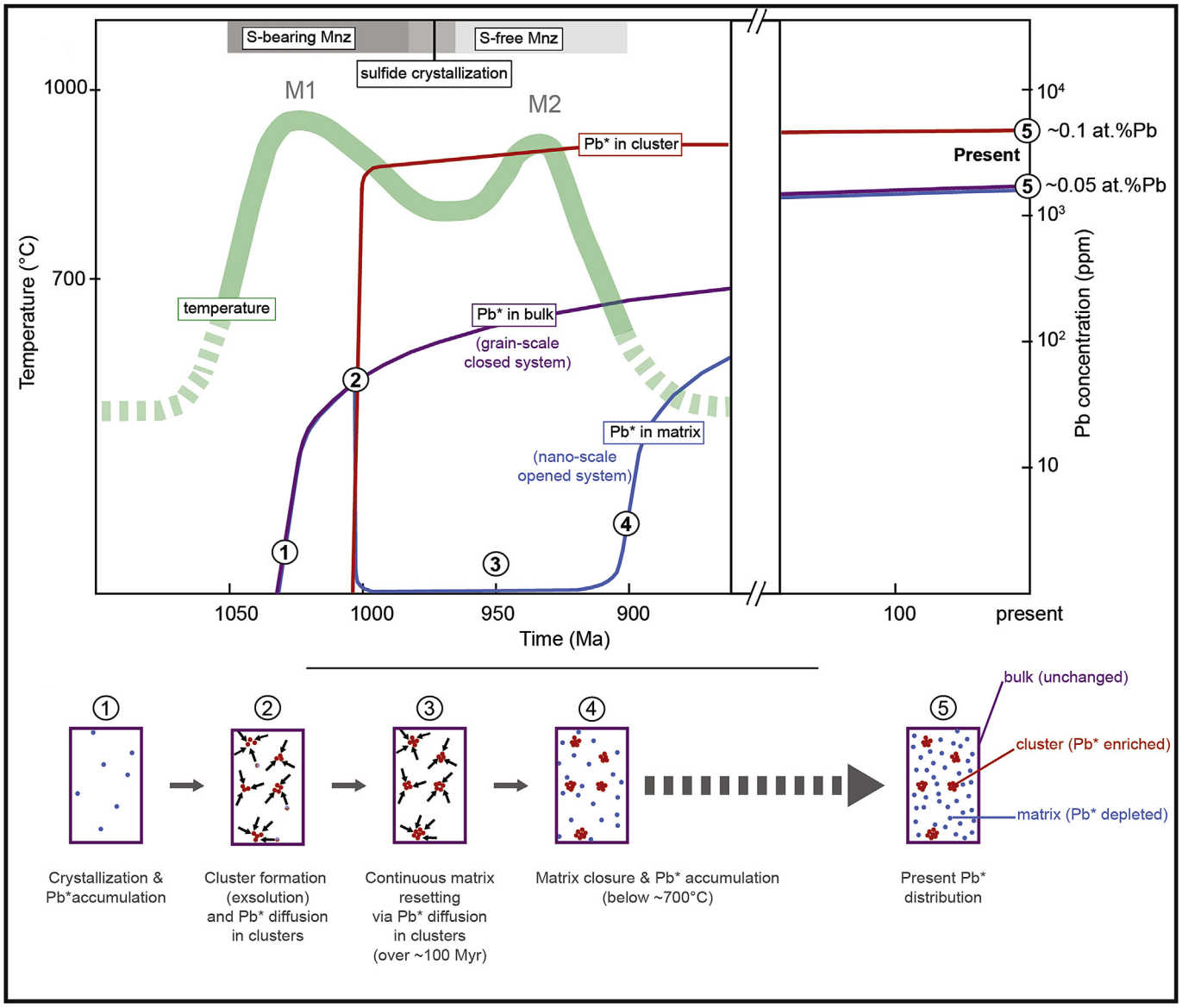


**Figure 7.** Schematic and interpretative history of the studied monazite crystal integrating data from Laurent et al. (2016) and the present study. Monazite grain crystallized during a first UHT phase (M1; >900 °C) at 1037 ± 19 Ma; no Pb is incorporated in its structure during crystallization, but Ca and S are incorporated as anhydrite component (Laurent et al., 2016). After crystallization, radiogenic Pb (Pb*) is produced from U and Th decays and starts to accumulate within the grain (purple curve, step 1). A slight cooling occurred after the first temperature peak, at around 1000 Ma (D2 monazite generation). The D1 monazite then intersects the solvus ($REEPO_4$-$CaSO_4$), resulting in homogenous exsolution of Ca–S-rich clusters (step 2) and the formation of two distinct reservoirs with different Pb composition and isotopic ratios at the nanoscale: the Pb* free matrix (blue curve) and the clusters (red curve). As $T > 800$ °C, all the Pb* produced since monazite crystallization is mobile and is instantaneously trapped within the clusters (step 2). Nanoscale diffusion of the produced Pb* (step 3) continued so that the monazite matrix was continuously reset until the final cooling following D3 where the system closed at around 700 °C (step 4). At this point, Pb* is immobile, even at the nanometre scale, and accumulates in the matrix (blue curve). Presently (step 5) D1 monazite display a concordant age of 1034 ± 6 Ma at the grain scale (purple), but with Pb*-enriched clusters (~0.1 at.% Pb) with aberrant old ages (>4 Ga) and Pb*-depleted matrix with ~100 Myr younger ages. Green curve: indicative temperature–time evolution deduced from temperature specific U–Pb geochronology (Y-in-monazite thermometry, Laurent et al., 2018a; Ti-in zircon thermometry, Laurent et al., 2018b) and $^{40}Ar$–$^{39}Ar$ geochronology on amphibole (Bingen et al., 1998).

700 °C during final cooling shortly after M2, since the durations required for Pb to diffuse over 25 nm are ~12 Myr and ~13 Gyr at 700 and 600 °C, respectively.

The integration of nanoscale structural, chemical and isotopic results from the present study with microscale constrains from previous studies (Laurent et al., 2016, 2018a) allows us to propose a complex geological story (Fig. 7) for the nanocluster bearing D1 monazite. The D1 domain crystallized at 1037 ± 19 Ma (step 1, Fig. 7) near UHT (>900 °C) conditions from a silicate melt, incorporating a $CaSO_4$ component (about 1.043 at.% Ca and 0.44 at.% S). After crystallization, radiogenic Pb (Pb*) is produced from U and Th decays and starts to accumulate within the bulk monazite (step 1, Fig. 7). A slight cooling occurred after the first temperature peak, at around 1000 Ma. The D1 monazite then intersects the solvus ($REEPO_4$-$CaSO_4$), resulting in homogenous exsolution of Ca–S-rich clusters (step 2, Fig. 7). Because temperature always remained above ~750–800 °C, all the Pb* produced since monazite crystallization was mobile and virtually instantaneously trapped in the clusters (step 2; Fig. 7). This process continued for the Pb* produced subsequently to cluster formation (step 3; Fig. 7), so that the monazite matrix was continuously reset until the final cooling following D3 where it closed at around 700 °C (step 4; Fig. 7). This produced D1 monazite with concordant age of 1034 ± 6 Ma at grain-scale (μscale), that are composed of Pb* enriched clusters with aberrant old ages and Pb* depleted matrix with ~100 Myr younger age.

It is worth noticing that only a sub-micrometric APM sampling of a single grain of D1 monazite would have already told us that the grain experienced a protracted metamorphic evolution starting at ~1.03 Ga, over a ~100 Ma duration and at temperatures above ~700 °C. This validates the powerfulness of APM and its ability in opening new opportunities in dating and timing geological processes.

### 5.4. The advantage of TEM–APM combination: toward correlative microscopy

Our results illustrate the consistency and complementarity between TEM and APM. There is a complete agreement between the TEM chemical data (Ce, P, Ca and S-line scan published in Laurent et al., 2016, and nano-chemical mapping Fig. 2) and APM data (proxigram in Fig. 5). Both techniques detect an enrichment in Ca, S and a depletion in P, Ce and Th in the nanoclusters compared to the matrix. Additionally, TEM show that the cluster interface with the host monazite is almost coherent, with only slight misorientation of the lattice (Fig. 2D). This structural information cannot be obtained with APM. On the other hand, APM can detect Pb at concentrations well below the TEM detection limit and demonstrates that clusters are enriched in Pb compared to the matrix. Moreover, the APM proxigram show that P and Ce are still present in the core of the nanoclusters, indicating that clusters are not a pure anhydrite phase but most probably a $(Ca,REE,Th,U,Pb)(S,P)O_4$ solid solution between the monazite ($LREEPO_4$) and anhydrite ($CaSO_4$) endmembers (Fig. 5). This cannot be deduced from TEM alone, which does not allow the selective analysis of ~10 nm clusters in a ~100 nm thick sample (transmission mode). In the present study, and to our knowledge, for the first time in geochronology, we overcome the weakness of each technique combining both on the same sample. The next step to go further would be to achieve TEM/APM correlative microscopy in geochronology, previously championed in material science (e.g. Grenier et al., 2015; Lefebvre-Ulrickson, 2016), biology (e.g. Langelier et al., 2017) and cosmochemistry (e.g. Rout et al., 2017).

## 6. Conclusions

Our study highlights that within a single microscale S-rich monazite core, phase separation led to the isolation of two different reservoirs at the nanoscale: a matrix (depleted in Pb*) and Ca–S-rich-nanoclusters (enriched in Pb*). Combining APM to TEM capabilities allows to (1) detect the presence of exsolved nanoclusters (5–10 nm in size) within S-rich monazite crystals; (2) reveal that nanoclusters are enriched in Pb of radiogenic origin; (3) specify the role of nanoclusters, which acts as a sink for the Pb* produced in the monazite over the ~100 Myrs of the high-T metamorphic evolution; (4) demonstrated closed U–Th–Pb geochronological systems at grain-scale (μscale) but opened systems at nano-scale where Pb diffusion cannot be neglected, and (5) provide the dating and timing of the thermal history of host rock. Geological interpretations in this case study are possible only because the Th–Pb geochronological system remained closed at the micrometre-scale as evidenced by the homogenous distribution of the clusters and their radiogenic-dominated Pb signature.

This study demonstrates that combining Atom Probe and Transmission Electron Microscopy is a new and powerful method for detailing the dating and timing of geological processes opening the way for nano-geochronology and nano-thermochronology.

## Acknowledgments

We thank Ph. De Parseval and S. Gouy for their technical assistance with the microprobe and Ioannis Alexandrou (FEI) for the TEM-EDS mapping. Both UJM and CNRS (INSU TelluS-SYSTER) are thanked for financial support for AMSG and ATL. The Australian Resource Characterisation Facility (ARCF), under the auspices of the National Resource Sciences Precinct (NRSP) – a collaboration between CSIRO, Curtin University and The University of Western Australia – is supported by the Science and Industry Endowment Fund (SIEF RI13-01).

## Appendix A. Supplementary data

Supplementary data to this article can be found online at https://doi.org/10.1016/j.gsf.2018.09.004.

## References

Ashwal, L.D., Tucker, R.D., Zinner, E.K., 1999. Slow cooling of deep crustal granulites and Pb-loss in zircon. Geochimica et Cosmochimica Acta 63, 2839–2851.

Bellucci, J.J., Nemchin, A.A., Whitehouse, M.J., Kielman, R.B., Snape, J.F., Pidgeon, R.T., 2018. Geochronology of Hadean zircon grains from the Jack Hills, Western Australia constrained by quantitative scanning ion imaging. Chemical Geology 476, 469–480.

Bingen, B., Boven, A., Punzalan, L., Wijbrans, J.R., Demaiffe, D., 1998. Hornblende 40Ar/39Ar geochronology across terrane boundaries in the Sveconorwegian Province of S. Norway. Precambrian Research 90, 159–185.

Bingen, B., Nordgulen, O., Viola, G., 2008. A four-phase model for the Sveconorwegian orogeny, SW Scandinavia. Norsk Geologisk Tidsskrift 88, 43.

Bingen, B., Stein, H., 2003. Molybdenite Re–Os dating of biotite dehydration melting in the Rogaland high-temperature granulites, S Norway. Earth and Planetary Science Letters 208, 181–195. https://doi.org/10.1016/S0012-821X(03)00036-0.

Bingen, B., Van Breemen, O., 1998. U-Pb monazite ages in amphibolite- to granulite-facies orthogneiss reflect hydrous mineral breakdown reactions: Sveconorwegian Province of SW Norway. Contributions to Mineralogy and Petrology 132, 336–353.

Black, L.P., Fitzgerald, J.D., Harley, S.L., 1984. Pb isotopic composition, colour, and microstructure of monazites from a polymetamorphic rock in Antarctica. Contributions to Mineralogy and Petrology 85, 141–148.

Blereau, E., Johnson, T.E., Clark, C., Taylor, R.J.M., Kinny, P.D., Hand, M., 2017. Reappraising the P–T evolution of the rogaland–vest agder sector, southwestern Norway. Geoscience Frontiers 8, 1–14.

Blum, T.B., Darling, J.R., Kelly, T.F., Larson, D.J., Moser, D.E., Perez-Huerta, A., Prosa, T.J., Reddy, S.M., Reinhard, D.A., Saxey, D.W., 2018. Best practices for reporting atom probe analysis of geological materials. Microstructural Geochronology: Planetary Records Down to Atom Scale 369–373.

Bonef, B., Gérard, L., Rouvière, J.L., Grenier, A., Jouneau, P.H., Bellet-Amalric, E., Mariette, H., André, R., Bougerol, C., 2015. Atomic arrangement at ZnTe/CdSe interfaces determined by high resolution scanning transmission electron microscopy and atom probe tomography. Applied Physics Letters 106, 051904.
Cherniak, D., Watson, E.B., Grove, M., Harrison, T.M., 2004. Pb diffusion in monazite: a combined RBS/SIMS study. Geochimica et Cosmochimica Acta 68, 829–840.
Cherniak, D.J., Watson, E.B., 2003. In: Hanchar, J.M., Hoskin, P.W.O. (Eds.), Diffusion in Zircon. Zircon. Mineralogical Soc Amer, Chantilly, pp. 113–143.
Clavier, N., Podor, R., Dacheux, N., 2011. Crystal chemistry of the monazite structure. Journal of the European Ceramic Society 31, 941–976.
Corfu, F., 2013. A century of U–Pb geochronology: the long quest towards concordance. The Geological Society of America Bulletin 125, 33–47.
Deschanels, X., Seydoux-Guillaume, A.M., Magnin, V., Mesbah, A., Tribet, M., Moloney, M., Serruys, Y., Peuget, S., 2014. Swelling induced by alpha decay in monazite and zirconolite ceramics: a XRD and TEM comparative study. Journal of Nuclear Materials 448, 184–194.
Drüppel, K., Elsasser, L., Brandt, S., Gerdes, A., 2013. Sveconorwegian mid-crustal ultrahigh-temperature metamorphism in Rogaland, Norway: U–Pb LA-ICP-MS geochronology and pseudosections of sapphirine granulites and associated paragneisses. Journal of Petrology 54 (2), 305–350.
Fougerouse, D., Reddy, S.M., Saxey, D.W., Erickson, T., Kirkland, C.L., Rickard, W.D.A., Seydoux-Guillaume, A.-M., Clark, C., Buick, I.S., 2018. Nanoscale distribution of Pb in monazite revealed by atom probe microscopy. Chemical Geology 479, 251–258. https://doi.org/10.1016/j.chemgeo.2018.01.020.
Fougerouse, D., Reddy, S.M., Saxey, D.W., Rickard, W.D., Van Riessen, A., Micklethwaite, S., 2016. Nanoscale gold clusters in arsenopyrite controlled by growth rate not concentration: evidence from atom probe microscopy. American Mineralogist 101, 1916–1919.
Gardés, E., Montel, J.-M., 2009. Opening and resetting temperatures in heating geochronological systems. Contributions to Mineralogy and Petrology 158, 185–195.
Gardés, E., Jaoul, O., Montel, J.-M., Seydoux-Guillaume, A.-M., Wirth, R., 2006. Pb diffusion in monazite: an experimental study of $Pb^{2+} + Th^{4+} \Leftrightarrow 2Nd^{3+}$ interdiffusion. Geochimica et Cosmochimica Acta 70 (9), 2325–2336.
Gardés, E., Montel, J.-M., Seydoux-Guillaume, A.-M., Wirth, R., 2007. Pb diffusion in monazite: new constraints from the experimental study of $Pb^{2+} \Leftrightarrow Ca^{2+}$ interdiffusion. Geochimica et Cosmochimica Acta 71 (16), 4036–4043.
Gault, B., Moody, M.P., Cairney, J.M., Ringer, S.P., 2012. Atom Probe Microscopy. Springer Science & Business Media.
Gault, B., Saxey, D.W., Ashton, M.W., Sinnott, S.B., Chiaramonti, A.N., Moody, M.P., Schreiber, D.K., 2016. Behavior of molecules and molecular ions near a field emitter. New Journal of Physics 18 (3), 033031.
Geisler, T., Rashwan, A.A., Rahn, M.K.W., Poller, U., Zwingmann, H., Pidgeon, R.T., Schleicher, H., Tomaschek, F., 2003. Low temperature hydrothermal alteration of natural metamict zircons from the Eastern Desert, Egypt. Mineralogical Magazine 67, 485–508.
Grand'Homme, A., Janots, E., Seydoux-Guillaume, A.M., Guillaume, D., Magnin, V., Hövelmann, J., Höschen, C., Boiron, M.C., 2018. Mass transport and fractionation during monazite alteration by anisotropic replacement. Chemical Geology 484, 51–68. https://doi.org/10.1016/j.chemgeo.2017.10.008.
Grand'Homme, A., Janots, E., Seydoux-Guillaume, A.-M., Guillaume, D., Bosse, V., Magnin, V., 2016. Partial resetting of the U–Th–Pb systems in experimentally altered monazite: nanoscale evidence of incomplete replacement. Geology 44 (6), 431–434.
Grenier, A., Duguay, S., Barnes, J.P., Serra, R., Haberfehlner, G., Cooper, D., Bertin, F., Barraud, S., Audoit, G., Arnoldi, L., Cadel, E., Chabli, A., Vurpillot, F., 2014. 3D analysis of advanced nano-devices using electron and atom probe tomography. Ultramicroscopy 136, 185–192.
Grenier, A., Duguay, S., Barnes, J.P., Serra, R., Rolland, N., Audoit, G., Morin, P., Gouraud, P., Cooper, D., Blavette, D., Vurpillot, F., 2015. Three dimensional imaging and analysis of a single nano-device at the ultimate scale using correlative microscopy techniques. Applied Physics Letters 106, 213102.
Hawkins, D., Bowring, S.A., 1997. U-Pb systematics of monazite and xenotime: case studies from the Paleoproterozoic of the Grand Canyon, Arizona. Contributions to Mineralogy and Petrology 127, 87.
Helmy, H.M., Ballhaus, C., Fonseca, R.O.C., Wirth, R., Nagel, T., Tredoux, M., 2013. Noble metal nanoclusters and nanoparticles precede mineral formation in magmatic sulphide melts. Nature Communications 4, 2405. https://doi.org/10.1038/ncomms3405.
Hellman, O.C., Vandenbroucke, J.A., Rüsing, J., Isheim, D., Seidman, D.N., 2000. Analysis of three-dimensional atom-probe data by the proximity histogram. Microscopy and Microanalysis 6 (05), 437–444.
Kelly, T.F., Larson, D.J., 2012. Atom probe tomography 2012. Annual Review of Materials Research 42, 1–31.
Kirkland, C., Erickson, T., Johnson, T., Danišík, M., Evans, N., Bourdet, J., McDonald, B., 2016. Discriminating prolonged, episodic or disturbed monazite age spectra: an example from the Kalak Nappe Complex, Arctic Norway. Chemical Geology 424, 96–110.
Kusiak, M.A., Wilde, S.A., Wirth, R., Whitehouse, M.J., Dunkley, D.J., Lyon, I., Reddy, S.M., Berry, A., deJonge, M., 2018. Detecting micro- and nanoscale variations in element mobility in high-grade metamorphic rocks: planetary records down to atom scale. In: Moser, D.E., Corfu, F., Darling, J.R., Reddy, S.M., Tait, K.T. (Eds.), Microstructural Geochronology: Planetary Records Down to Atom Scale, vol. 232. AGU/Wiley Publishing, pp. 279–291.
Kusiak, M.A., Dunkley, D.J., Wirth, R., Whitehouse, M.J., Wilde, S.A., Marquardt, K., 2015. Metallic lead nanospheres discovered in ancient zircons. Proceedings of the National Academy of Sciences of the United States of America 112, 4958–4963.
Kusiak, M.A., Whitehouse, M.J., Wilde, S.A., Nemchin, A.A., Clark, C., 2013. Mobilization of radiogenic Pb in zircon revealed by ion imaging: implications for early Earth geochronology. Geology 41, 291–294.
Langelier, B., Wang, X., Grandfield, K., 2017. Atomic scale chemical tomography of human bone. Scientific Reports 7, 39958. https://doi.org/10.1038/srep39958.
Laurent, A.T., Duchene, S., Bingen, B., Bosse, V., Seydoux-Guillaume, A., 2018a. Two successive phases of ultrahigh temperature metamorphism in Rogaland, S. Norway: evidence from Y-in-monazite thermometry. Journal of Metamorphic Geology. https://doi.org/10.1111/jmg.12425.
Laurent, A.T., Bingen, B., Duchene, S., Whitehouse, M.J., Seydoux-Guillaume, A.-M., Bosse, V., 2018b. Decoding a protracted zircon geochronological record in ultrahigh temperature granulite, and persistence of partial melting in the crust, Rogaland, Norway. Contribution to Mineralogy and Petrology 173, 29. https://doi.org/10.1007/s00410-018-1455-4.
Laurent, A.T., Seydoux-Guillaume, A.-M., Duchene, S., Bingen, B., Bosse, V., Datas, L., 2016. Sulphate incorporation in monazite lattice and dating the cycle of sulphur in metamorphic belts. Contributions to Mineralogy and Petrology 171 (11), 94.
Lefebvre-Ulrickson, W., 2016. In: Lefebvre-Ulrikson, W., Vurpillot, F., Sauvage, X. (Eds.), Chapter in Book "Atom Probe Tomography: Put Theory into Practice". Academic Press, Elsevier, pp. 319–352. ISBN-10: 0128046473.
Möller, A., O'brien, P.J., Kennedy, A., Kröner, A., 2002. Polyphase zircon in ultrahigh-temperature granulites (Rogaland, SW Norway): constraints for Pb diffusion in zircon. Journal of Metamorphic Geology 20, 727–740.
Montel, J.-M., Devidal, J.-L., Avignant, D., 2002. X-ray diffraction study of brabantite-monazite solid solution. Chemical Geology 191, 89–104.
Montel, J.-M., Foret, S., Veschambre, M., Nicollet, C., Provost, A., 1996. Electron microprobe dating of monazite. Chemical Geology 131, 37–53.
Ni, Y., Hughes, J.M., Mariano, A.N., 1995. Crystal chemistry of the monazite and xenotime structures. American Mineralogist 80, 21–26.
Peterman, E.M., Reddy, S.M., Saxey, D.W., Snoeyenbos, D.R., Rickard, W.D., Fougerouse, D., Kylander-Clark, A.R., 2016. Nanogeochronology of discordant zircon measured by atom probe microscopy of Pb-enriched dislocation loops. Science Advances 2 (9), e1601318.
Piazolo, S., La Fontaine, A., Trimby, P., Harley, S., Yang, L., Armstrong, R., Cairney, J.M., 2016. Deformation induced trace element redistribution in zircon revealed using atom probe tomography. Nature Communications 7, 10490.
Ramasse, Q.M., 2017. Twenty years after: how "Aberration correction in the STEM" truly placed a "A synchrotron in a Microscope". Ultramicroscopy 180, 41–51.
Reddy, S.M., van Riessen, A., Saxey, D.W., Johnson, T.E., Rickard, W.D.A., Fougerouse, D., Olson, D., 2016. Mechanisms of deformation-induced trace element migration in zircon resolved by atom probe and correlative microscopy. Geochimica et Cosmochimica Acta 195, 158–170. https://doi.org/10.1016/j.gca.2016.09.019.
Reiner, P.W., Ehlers, T.A. (Eds.), 2005. Low-temperature Thermochronology: Techniques, Interpretations, and Applications. Reviews in Mineralogy & Geochemistry, vol. 58. Mineralogical Society of America, p. 622.
Rout, S.S., Heck, P.R., Isheim, D., Stephan, T., Zaluzec, N.J., Miller, D.J., Davis, A.M., Seidman, D.N., 2017. Atom-probe tomography and transmission electron microscopy of the kamacite-taenite interface in the fast-cooled Bristol IVA iron meteorite. Meteoritics and planetary science 52, 2707–2729.
Saxey, D., Reddy, S.M., Fougerouse, D., Rickard, W.D., 2018. The optimization of zircon analyses by laser-assisted atom probe microscopy: Insights from the 91500 zircon standard. Microstructural Geochronology: Planetary Records Down to Atom Scale 293–313.
Seydoux-Guillaume, A.-M., Bingen, B., Paquette, J.L., Bosse, V., 2015. Nanoscale evidence for uranium mobility in zircon and the discordance of U–Pb chronometers. Earth and Planetary Science Letters 409, 43–48.
Seydoux-Guillaume, A.-M., Bingen, B., Bosse, V., Janots, E., Laurent, A.T., 2018a. Transmission Electron Microscope imaging sharpens geochronological interpretation of zircon and monazite. In: Moser, D.E., Corfu, F., Darling, J.R., Reddy, S.M., Tait, K.T. (Eds.), Microstructural Geochronology: Planetary Records Down to Atom Scale, vol. 232. AGU/Wiley Publishing, pp. 261–275.
Seydoux-Guillaume, A.-M., Deschanels, X., Baumier, C., Neumeier, S., Weber, W.J., Peuget, S., 2018b. Why natural monazite never becomes amorphous: experimental evidence for alpha self-healing. American Mineralogist 103, 824–827. https://doi.org/10.2138/am-2018-6447.
Seydoux-Guillaume, A.-M., Goncalves, P., Wirth, R., Deutsch, A., 2003. Transmission electron microscope study of polyphase and discordant monazites: site-specific specimen preparation using the focused ion beam technique. Geology 31 (11), 973–976.
Seydoux-Guillaume, A.-M., Montel, J.-M., Bingen, B., Bosse, V., De Parseval, P., Paquette, J.-L., Janots, E., Wirth, R., 2012. Low-temperature alteration of monazite: fluid mediated coupled dissolution–precipitation, irradiation damage, and disturbance of the U–Pb and Th–Pb chronometers. Chemical Geology 330, 140–158.
Seydoux-Guillaume, A.-M., Wirth, R., Deutsch, A., Schärer, U., 2004. Microstructure of 24-1928 Ma concordant monazites: Implications for geochronology and nuclear waste deposits. Geochimica et Cosmochimica Acta 68, 2517–2527.
Seydoux-Guillaume, A.-M., Wirth, R., Nasdala, L., Gottschalk, M., Montel, J.M., Heinrich, W., 2002. An XRD, TEM and Raman study of experimentally annealed natural monazite. Physics and Chemistry of Minerals 29, 240–253.

Slagstad, T., Roberts, N.M.W., Marker, M., Røhr, T.S., Schiellerup, H., 2013. A non-collisional, accretionary Sveconorwegian orogen. Terra Nova 25, 30–37. https://doi.org/10.1111/ter.12001.

Smye, A.J., Stockli, D.F., 2014. Rutile U-Pb and depth profiling: a continuous record of lithospheric thermal evolution. Earth and Planetary Science Letters 408, 171–182.

Stacey, J.t., Kramers, J., 1975. Approximation of terrestrial lead isotope evolution by a two-stage model. Earth and Planetary Science Letters 26 (2), 207–221.

Thompson, K., Lawrence, D., Larson, D., Olson, J., Kelly, T., Gorman, B., 2007. In situ site-specific specimen preparation for atom probe tomography. Ultramicroscopy 107 (2), 131–139.

Valley, J.W., Cavosie, A.J., Ushikubo, T., Reinhard, D.A., Lawrence, D.F., Larson, D.J., Clifton, P.H., Kelly, T.F., Wilde, S.A., Moser, D.E., 2014. Hadean age for a post-magma-ocean zircon confirmed by atom-probe tomography. Nature Geoscience 7 (3), 219–223.

Valley, J.W., Reinhard, D.A., Cavosie, A.J., Ushikubo, T., Lawrence, D.F., Larson, D.J., Kelly, T.F., Snoeyenbos, D.R., Strickland, A., 2015. Presidential Address. Nano- and micro-geochronology in Hadean and Archean zircons by atom-probe tomography and SIMS: new tools for old minerals. American Mineralogist 100 (7), 1355–1377.

Villa-Vialaneix, N., Montel, J.-M., Seydoux-Guillaume, A.-M., 2013. NiLeDAM: Monazite Datation for the NiLeDAM Team. R Package Version 0.1. http://niledam.r-forge.r-project.org.

Vurpillot, F., Bostel, A., Blavette, D., 2000. Trajectory overlaps and local magnification in three-dimensional atom probe. Applied Physics Letters 76 (21), 3127–3129.

Weber, J., Barthel, J., Brandt, F., Klinkenberg, M., Breuer, U., Kruth, M., Bosbach, D., 2016. Nano-structural features of barite crystals observed by electron microscopy and atom probe tomography. Chemical Geology 424, 51–59.

Wetherill, G.W., 1956. Discordant uranium-lead ages 1. Transactions - American Geophysical Union 37, 320–326.

White, L.F., Darling, J., Moser, D., Reinhard, D., Prosa, T., Bullen, D., Olsen, D., Larson, D., Lawrence, D., Martin, I., 2017. Atomic-scale age resolution of planetary events. Nature Communications 8, 1–6.

Whitehouse, M.J., Kumar, G.R.R., Rimša, A., 2014. Behaviour of radiogenic Pb in zircon during ultrahigh-temperature metamorphism: an ion imaging and ion tomography case study from the Kerala Khondalite Belt, southern India. Contributions to Mineralogy and Petrology 168, 1–18.

Whitehouse, M.J., Kusiak, M.A., Wirth, R., Ravindra Kumar, G.R., 2017. Metallic Pb nanospheres in ultra-high temperature metamorphosed zircon from southern India. Mineralogy and Petrology 111, 467–474.